Rock Mechanics and Rock Engineering (2024) 57:2661–2680
https://doi.org/10.1007/s00603-023-03704-6

ORIGINAL PAPER

Advancing Geotechnical Analysis with Octree-based Processing: Voxel-Level Integration of Mobile Laser Scanning Data, Geological Models, and Microseismic Data

Lukas Fahle[1] · Andrew J. Petruska[1] · Gabriel Walton[1] · Jurgen F. Brune[1] · Elizabeth A. Holley[1]

Received: 4 September 2023 / Accepted: 28 November 2023 / Published online: 8 January 2024

Abstract

This study introduces an enhanced octree-based framework for integrated geotechnical analysis, combining geological, microseismic, and Mobile Laser Scanning (MLS)-based change detection data. Our approach leverages efficient statistical inference-based change detection techniques and additional octree data structures, enabling voxel-level data integration and association, semantic clustering, and comprehensive geotechnical analysis. We detail the implementation of our method, demonstrating capabilities such as integrating geological fault data, seismic energy exposure modeling, and combination of Random Sample Consensus (RANSAC) classification with Density-Based Spatial Clustering of Applications with Noise (DBSCAN). We conduct a suite of statistical analyses to investigate multi-dimensional trends and correlations among MLS-measured changes, distances to geological faults, and seismic energy exposure. We found that binary change classification and change magnitude negatively correlate with three investigated fault-distance metrics. Multivariant analysis reveals that increased seismic energy exposure and decreased fault distance positively correlates with MLS-based change classification and magnitudes. Our findings imply that proximity to geological faults and seismic energy exposure can be statistically linked to increases in geotechnically relevant deformations. This study is the first to demonstrate that octree-based MLS data processing can reveal multi-dimensional trends in underground mine datasets, thereby enhancing understanding of complex geomechanical behaviors crucial for mining productivity and safety.

Highlights

- Introduced octree-based framework for integrated geotechnical analysis.
- Combined geological, microseismic, and MLS data at voxel level.
- Utilized statistical inference for change detection in framework.
- Found correlations between MLS changes, fault proximity, and seismic energy.

Keywords Mobile laser scanning · Integrated geotechnical analysis · Octree data structures · Change detection · RANSAC and DBSCAN · Seismic energy

1 Introduction

The excavation and operation of underground openings such as caverns, tunnels, and mining drifts results in the redistribution of stress fields in the surrounding rockmass (Terzaghi 1942). In mining, stress-related rockmass failure is defined by fracturing or disintegration, resulting in loss of bearing capacity and structural damage. Geotechnical precursors of structural damage include ground deformations, deteriorating ground conditions, and uncontrolled ground movement, including convergence, fall of ground, seismicity, and rock bursts (Szwedzicki 2001). These are significant hazards to both personnel and physical assets in underground spaces (Mark and Molinda 2004; Li et al. 2008; Palei and Das

✉ Lukas Fahle
lukasfahle@mines.edu

[1] Colorado School of Mines, Golden, CO, USA

2008; Kaiser and Cai 2012; Nordlund 2013; Sandbak and Rai 2013; Oraee et al. 2016; Ma et al. 2020a; Zhao et al. 2022; Hu et al. 2022).

Geotechnical monitoring and ground control measures are implemented to detect and prevent convergence and fall of ground, thus ensuring safety, operational reliability, and economic viability in underground mines. Visual inspections and in-situ instrumentation (e.g., multi-point borehole extensometers) are commonly applied tools for ground monitoring. More recently, lidar-based Simultaneous Localization and Mapping (SLAM) Mobile Laser Scanning (MLS) systems have shown to be useful in enabling frequent, mine-wide geotechnical monitoring due to significantly higher data acquisition efficiency than traditional inspections. (Williams et al. 2013; Puente et al. 2016; Raval et al. 2019). Fahle et al. (2021, 2022) showed that multi-epoch MLS data could detect geotechnical hazards while achieving high data quality with uncertainty on the millimeter-to-centimeter level when utilizing the multi-scale model-to-model cloud comparison (M3C2) algorithm (Lague et al. 2013).

To retain high data quality and address the computational limitations of M3C2 for application to large data sets, we previously described an MLS-monitoring framework built on an octree data structure that enabled change detection via intra-voxel statistical inference (Fahle et al. 2023). Our approach facilitates real-time geotechnical change detection on a mine scale. One of the remaining limitations of MLS-based geotechnical monitoring is the integration of change detection with relevant geotechnical metadata to interpret trends and underlying causes of deformation. Geological structures and seismic activity are two examples of metadata correlated to geotechnical changes. Geological structures such as fractures, joints, and faults can significantly affect the rockmass behavior and, therefore, the development of convergence and falls of ground (Szwedzicki 2001; Trifu and Suorineni 2009; Wang et al. 2018). Faults have been identified as particularly relevant geological structures in rockmass failures (Brekke and Selmer-Olsen 1966; Suorineni et al. 1999). Open-stope mining methods deployed in metalliferous orebodies are frequently associated with fault-induced failures (Dunne and Pakalnis 1996; Bruneau et al. 2003b, a; Mikula 2020; Xia et al. 2022).

Today, many underground hard-rock mines utilize passive seismic sensor systems to monitor mining-induced seismicity. Mining-induced seismicity and passive seismic tomography have been used for stress distribution studies, forecasting of rock bursts, and improving mine safety (Young and Maxwell 1992; Meglis et al. 2005; Mercer and Bawden 2005; Luxbacher et al. 2008; Ma et al. 2016, 2020b; Westman et al. 2017; Leake et al. 2017; Vatcher et al. 2018). A significant increase in the frequency or concentration of seismic events can indicate impending rock failures (Goebel et al. 2015). Like other in-situ instrumentation, seismic sensors can only capture events within a certain vicinity of the sensor array, which might result in incomplete data. For example, Slaker et al. (2020) captured underground mine deformation with stationary, terrestrial laser scanning (TLS) although no associated seismic events could be recorded. Kumar (2022) suggested that lidar data could be combined with other sensors, such as seismic, stress, and extensometers, to provide early warnings of potential geotechnical hazards. Therefore, we posit that seismic data could be useful metadata to supplement MLS-based change detection and deformation monitoring.

Although many studies document correlations among geological structures, seismicity, and rockmass behavior, challenges remain in the systematic integration of these factors into a unified analysis. Traditional geotechnical analyses comprise field and desktop investigations of observations of rockmass behavior and its relationship to geological features and properties. Desktop analysis usually involves the visualization of monitoring and geological data in different software tools and may include various manual data processing and manipulation steps. However, this approach is time consuming and does not fully utilize the data's digital properties. Furthermore, such approaches commonly preclude automated correlation of multiple types of geotechnical data. With the increasing proliferation of MLS-based rockmass monitoring and the resulting large volume of spatiotemporal data, these limitations in geotechnical analyses are further exacerbated. We are unaware of any attempts to perform a low-level integration of MLS-based change detection and geological and seismological data in a unified framework.

This study utilizes our previously proposed (Fahle et al. 2023) voxel framework to incorporate geotechnical relevant metadata. Using this approach, we demonstrate an integrated geotechnical monitoring framework using MLS, geological, and seismic field data from Glencore Kidd Mine in Ontario, Canada. We also improve our data-processing pipeline using advanced clustering and fully parallelized ray-casting-based seismic energy computation. The paper makes the following contributions:

- Demonstration of a novel approach for integrated MLS-based geotechnical monitoring using geological and seismic data
- Analysis of MLS field data from Kidd Mine, including identification of statistically significant differences in change detection results based on spatial correlation with geological and seismological data.
- Improve automation of change detection workflow by implementing a combined RANSAC and DBSCAN segmentation and clustering approach

2 Materials and Methods

2.1 Kidd Mine and Case Study Data

The Kidd copper and zinc mine is located 27 km north of Timmins in Ontario, Canada. With a maximum depth of 3063 m, Kidd Mine is the world's deepest base-metal mine. Mining at Kidd uses two shafts and blasthole stoping with pastefill as a mining method to move more than 4900 tonnes of material per day. The deposit is located in the Archaean Abitibi greenstone belt. Ore is hosted in the Kidd Volcanic Complex, a steeply dipping volcanogenic sulfide deposit cut by mafic sills and dykes. In this setting, geological faults and joint structures have been linked to seismic events and geotechnical failures (Suorineni et al. 1999; Counter 2014, 2019). Click or tap here to enter text.

Stresses on faults at Kidd Mine are influenced by interconnected "domino-like" effects of close and far-field rockmass deformations (Ma et al. 2020b). These deformations can cause incremental slips on major faults and sudden structural failures. Such abrupt failures can compromise the structural integrity of openings such as stopes and drifts. Various studies have also highlighted the bidirectional causality of seismic events and excavation deformations (Urbancic and Trifu 2000; Ma et al. 2020b; Zhen et al. 2022). Seismicity at Kidd Mine is often linked to active geological fault systems (Disley 2014; Counter 2019; Ma et al. 2020b). As such, Kidd Mine constantly strives to improve the understanding of MLS-measured deformations, geological structures, and seismic behavior to defray the additional geotechnical risks associated with deepening the mine. For example, Kidd's seismicity data is, among other things, used to establish safe re-entry protocols for restricted areas after blasting or significant seismic events (Disley 2014). While this approach has been proven beneficial, Disley (2014) also highlights the potential of supplementing seismic data with additional information, including proximity to major faults and geometric changes in the mine drifts. Our study adopts the suggestion of Ma et al. (2020b) to consider energy release as a metric for evaluating seismic events, in addition to the seismic event rate.

The Kidd Mine geotechnical team collected and provided the two MLS datasets used in this study (Fig. 1). The scans were collected with a GeoSlam ZEB Revo and Horizon scanner and processed within GeoSlam's SLAM software. They were georeferenced and aligned using ICP (Iterative Closest Point) methods within the Cloud Compare software (CloudCompare 2021). Two scans of the 9800 Level Access were performed on 07/31/2020 and 11/24/2020, with an intervening time period of 3 months and 24 days. We also utilize two scans of the 6700-01S level performed on 07/12/2018 and 03/28/2022, with an intervening period of almost 4 years. We utilize mining-induced seismicity data recorded via a microseismic monitoring system that included 8 triaxial stations and 23 uniaxial stations developed by ESG Solutions. Kidd Mine's seismic monitoring system is described in more detail by Ma et al. (2020b). We utilized a subset of the data that included seismic events that occurred within the same time interval as the analyzed MLS data. The data were provided as a processed database, including 47,666 seismic events between January 2017 and June 2022 with their timestamp, x, y, z-coordinates, and seismic energy

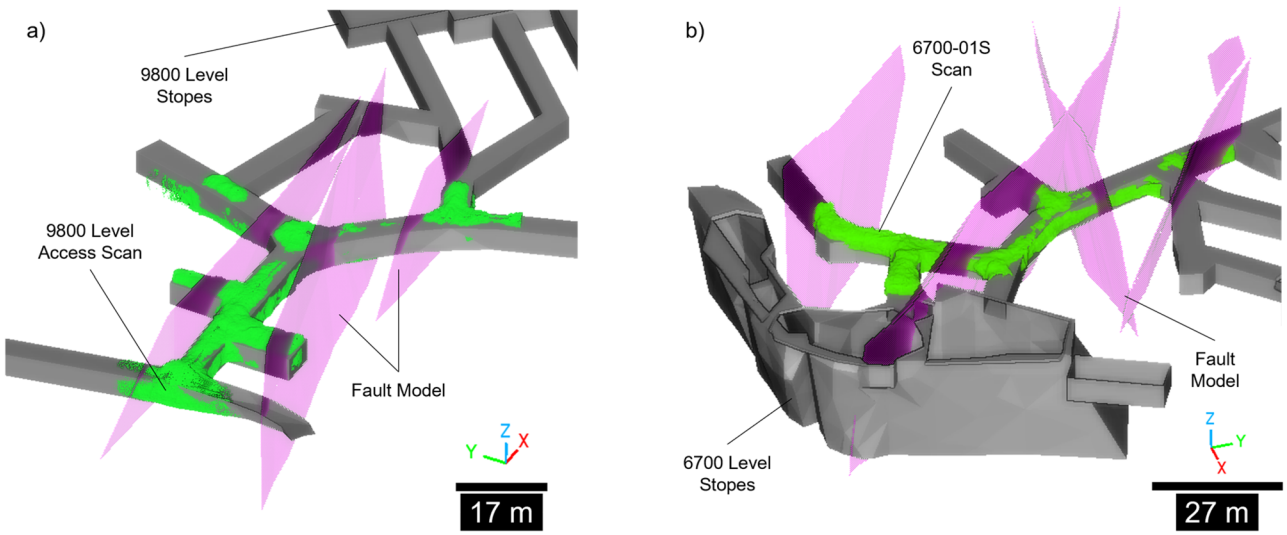

Fig. 1 Overview of MLS data collected at Kidd Mine underground mine on 9800 Level Access (**a**) and 6700-01S (**b**) using a GeoSlam ZEB Revo with overlayed geological fault model

released. We also utilized a geological dataset containing the major fault groups at Kidd Mine provided as meshed solids in a ply data format.

2.2 Octree-based Inference Change Detection and Voxel Augmentation

An octree is a hierarchical data structure that divides 3D space into nodes (Meagher 1982; Wilhelms and van Gelder 1992). Nodes are commonly represented by cubical volumes referred to as voxels. Each voxel can be recursively divided into eight smaller sub-sections until a minimum voxel size or tree depth is reached. The minimum voxel size $l_{\min}$ determines the octree's level of detail or resolution, with lower values representing higher resolutions. To analyze changes in our datasets, we utilize our previously described octree data structure and statistical inference-based change detection framework (Fahle et al. 2022). Our octrees based on MLS Cloud Epoch 1 (E1) and Epoch 2 (E2) are supplemented with summary statistics of the lidar points falling within each voxel. These include each voxel's mean x, y, and z in the mean vector x and a 3×3 covariance matrix Σ. These statistics describe the sampled surfaces in more detail than a voxel, which usually only represents occupied, unoccupied, or unknown space (Fig. 2).

Traditional change detection methods rely on distance computations via cloud-to-cloud (C2C), cloud-to-mesh (C2M), or multi-scale model-to-model cloud comparison (M3C2) algorithms. In our approach, we utilize per-voxel summary statistics for statistical inference classification via Chi-Squared tests and a common significance level $\alpha = 0.05$ to estimate the probability of an outcome (such as geotechnically-relevant changes) based on the frequency of findings supporting this outcome (such as distance differences between two MLS epochs). Our statistical test then quantitatively assesses the probability of measured changes being statistically significant and classifies voxels into significant and non-significant changes. To reduce the Chi-Square test's sensitivity to sample size, we enforce a minimum sample size of $n_{\min} = 30$ (Schiefer and Schiefer 2021). Based on our average MLS point spacing of 0.01 m and testing, we found that $l_{\min}$ of 0.5 m returns about 2000 point-pairs for each Chi-Squared test. This voxel size guarantees sufficient samples even in lower-density scan areas and provides a sub-sampled output for efficient geotechnical correlation analysis.

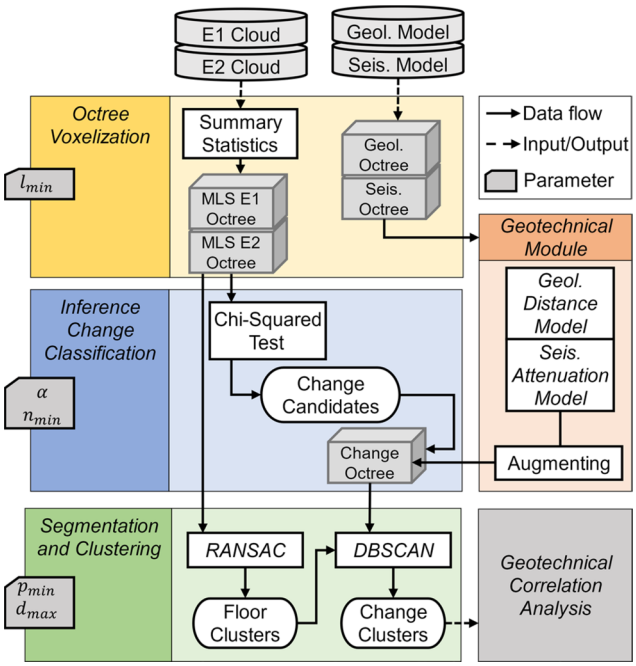

Fig. 3 Schematic overview of our framework for integrating MLS, geological fault, and seismic data to output data for geotechnical correlation analysis

2.3 Geological Fault Distance Computations

After performing inference change classification using our MLS data epochs E1 and E2, we augment the MLS octree voxels of classified changes by correlating the geological

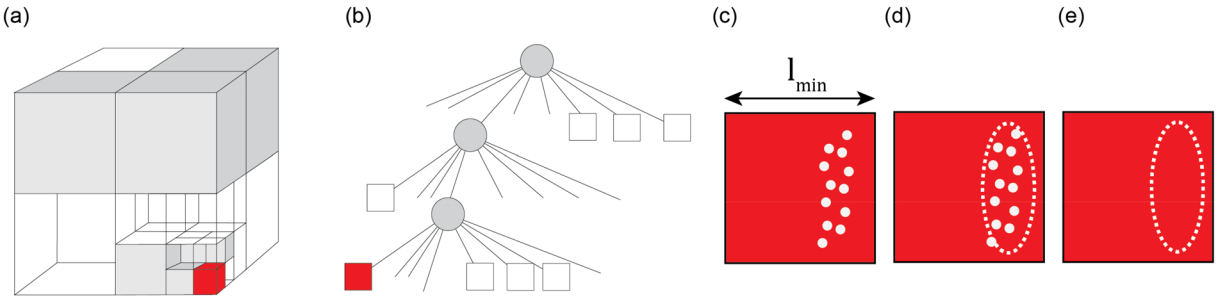

Fig. 2 Schematic of a volumetric (**a**) and tree (**b**) representation of an octree structure storing Boolean occupancy free (white) and occupied (grey). Example of an occupied voxel of size $l_{\min}$ storing MLS points of a surface (**c**), a graphical representation of the covariance of the points (**d**), and the data maintained in our octree (**e**)

and seismic model data provided by Kidd Mine, as summarized in Fig. 3.

The octrees for geological fault and seismic data integration utilize the same $l_{\min}$ octree resolution as the MLS octrees. While selecting different octree resolutions for each data type is possible, we chose to maintain a resolution for geological and seismic data consistent with our MLS octree resolution. This resolution balances computational performance with sufficient accuracy to represent the original fault model with a triangle side length between 5–30 m. We utilize a voxel-triangle intersection test to perform octree voxelization on the 3D-triangular mesh model of geological faults (Möller 1997). We can then associate voxels in our MLS data octrees with geological metadata by performing efficient octree nearest-neighbor searches. This approach enables various operations to generate quantitative models correlating MLS-monitoring data and geological information such as fault zones.

As highlighted in our review of other studies, geological faults can significantly influence rockmass behavior and geometric changes within the mine drift. One metric that likely plays a critical role is the spatial distance of fault zones to a given region of the mine drifts. To analyze our MLS-based change detection, we derive three different distance metrics for each MLS voxel, as shown in Fig. 4:

A. the shortest Euclidian distance between an MLS voxel and the closest intersection of a fault voxel with an MLS voxel,
B. the shortest connected voxel-to-voxel path (Dijkstra 1959) between an MLS voxel and the intersection of a fault voxel with an MLS voxel, and
C. the shortest Euclidian distance between an MLS voxel and any fault voxel—not necessarily requiring an intersection with an MLS voxel.

To evaluate the potential correlation between MLS-measured changes and geological faults, we provide boxplots and derive parametric [mean, standard deviation (SD)] and non-parametric summary statistics [median, mean average deviation (MAD)] for voxels with and without statistically significant change ("changed" and "unchanged", respectively). We evaluate the statistical significance of the correlation between MLS changes and geological fault data using a common 0.05 significance level and a non-parametric Mann–Whitney U test (Mann and Whitney 1947). We also use linear regression modeling to investigate the correlation between dependent (MLS-measured change) and independent (distance to fault) variables.

2.4 Seismic Energy Computation

To estimate the influence of seismic events on geometric changes observed in the MLS data, we approximate the energy E_R received by each MLS voxel. We use a simplified geometric attenuation model (Lowrie 2007), assuming that the initial energy E_0 at a given distance r from the seismic source is distributed over the surface of a sphere:

$$E_{R_{\text{Geometric}}} = \frac{E_0}{4\pi r^2}.$$

In addition to geometric attenuation, anelastic damping causes further loss of seismic wave energy (e.g., by conversion into heat). The wavelength-dependent quality factor (Q) describes this damping effect which is more pronounced in low-stiffness solids (Lowrie 2007) and less pronounced in an intact rockmass with fewer open joints, less clay, and reduced frequency of jointing (Barton 2007). In addition to geometric attenuation, scattering is a phenomenon that occurs when seismic waves interact with heterogeneities in fault zones, such as fractures, damage zones, and low-velocity layers. Scattering can produce effects such as attenuation, reverberation, trapped waves, and noise (Hamilton and Mooney 1990; Shapiro and Kneib 1993; Hillers et al. 2014; Touma et al. 2022; King et al. 2022). Fault-related scattering, therefore, also causes additional attenuation of seismic wave energy. Due to the significance of geological structures

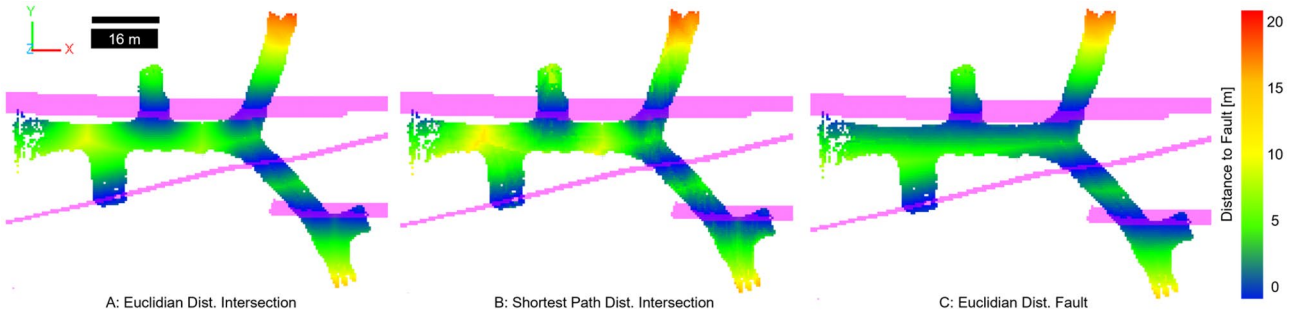

Fig. 4 Three distance metrics for Kidd Mine MLS and geological fault data at the 9800 Level Access: **A** Euclidian distance to the closest fault-voxel intersection, **B** Shortest connected path to a fault-voxel intersection, **C** Euclidian distance to closest fault voxel

at Kidd Mine, we tested an attenuation model based on the assumption that the disturbed rockmass within a fault zone increases energy attenuation. We model this increase in attenuation based on the travel distance of a seismic wave through a fault zone.

Figure 5 provides an overview of a simple implementation of a combined model considering geometric attenuation in all voxels and scattering attenuation in fault zones. First, seismic data, including date and total radiated energy, are stored in an octree at 0.5 m voxel resolution. The cumulative released energy between 2 time periods of interest (e.g., MLS scan dates) is stored if multiple events fall within the same voxel. We then cast a ray from each seismic voxel to each MLS voxel to compute its energy exposure. If the ray intersects a geological fault voxel, we can modify the geometric attenuation function $f(\lambda_g)$ with a scattering component $f(\lambda_g + \lambda_s)$. In our model, we modify the geometric attenuation function by increasing the exponent of r based on the number of fault voxels intersected by the ray n to calculate the combined effects of geometric and scattering attenuation on the received energy $E_{R_{\text{Combined}}}$:

$$E_{R_{\text{Combined}}} = \frac{E_0}{4\pi r^{(2+\frac{n}{20})}}.$$

In our model, we increased r by 0.05 for each intersecting voxel to achieve a reasonable attenuation based on testing. This study is more focused on discovering relative trends rather than the absolute energy. Future studies should consider more detailed analysis and calibration should be considered. The more fault voxels a ray intersects between its seismic event origin to its MLS voxel destination, the larger the exponent of r becomes, effectively increasing the attenuation effect. The estimated cumulative energy received by each MLS voxel E_R is incremented based on the respective attenuation function.

Figure 6 shows example outputs of our seismic models. In Fig. 6a, only geometric attenuation is computed, and the seismic energy exposure decreases quadratically with distance from the event distance. If scattering is incorporated, the model implements the attenuation based on the number of fault voxels passed to reach an MLS voxel, as shown in Fig. 6b. We analyze potential correlations between seismic energy exposure and MLS-measured changes following the methodology described for geological fault data.

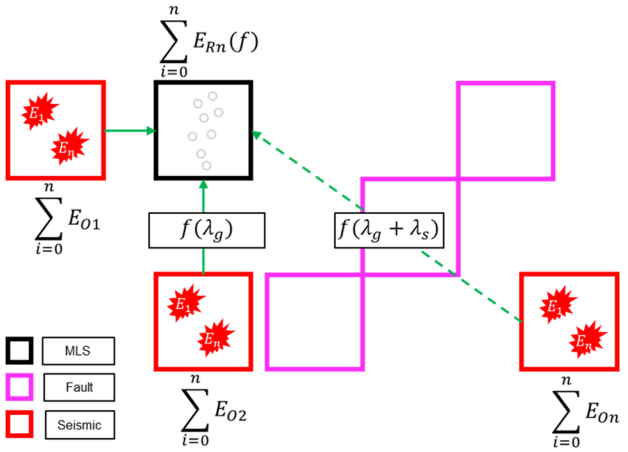

Fig. 5 Schematic of prototype seismic energy attenuation model

2.5 Improved Clustering Using RANSAC and DBSCAN

Our previous work utilized a K-nearest-neighbor algorithm to cluster adjacent MLS voxels with detected changes (Fahle et al. 2023). This approach was effective in initial tests with relatively few artificially introduced changes. In tests on

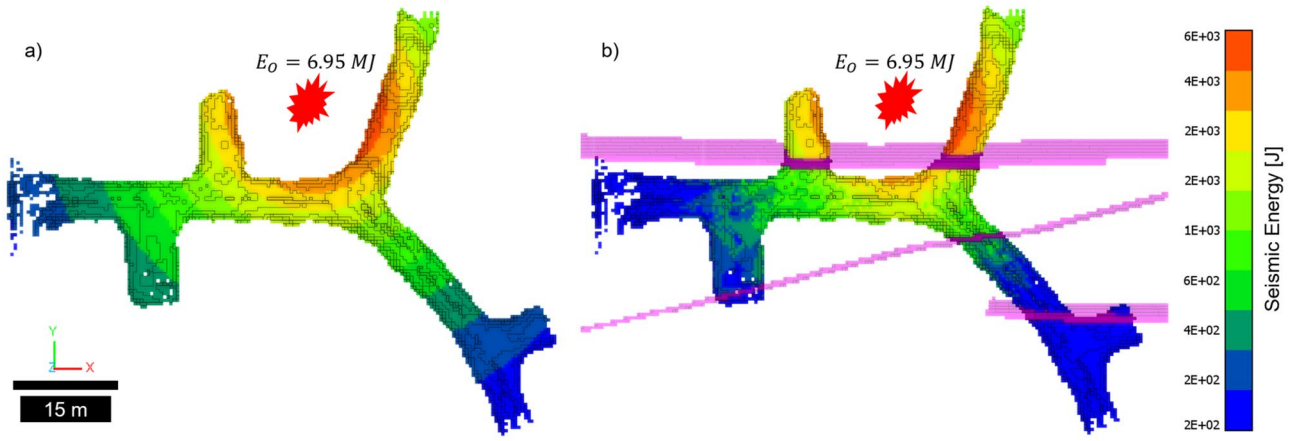

Fig. 6 Example of seismic energy attenuation model output with MLS data using only geometric attenuation (**a**) and with fault model for combined geometric and scattering attenuation (**b**). Energy release E_O is comparable to a 1.0 Local Magnitude (ML) event at Kidd Mine

Kidd Mine data, we found its performance on datasets that span longer time intervals between MLS scans and include a larger number of changes to be insufficient. The primary limitation of our initial implementation was the inability to specify the minimum number of points required to form a cluster. This caused the algorithm to generate many small, fragmented clusters, making it difficult to identify meaningful changes in the data.

Density-based spatial clustering of applications with noise (DBSCAN) (Ester et al. 1996) has shown promising results for rockfall detection in high-density static terrestrial lidar datasets (Tonini and Abellan 2014; DiFrancesco et al. 2020). In our adaptation of DBSCAN we use a maximum search radius r_{max} and a minimum number of voxels v_{min} to define a cluster (Fig. 7). As described by van Veen et al. (2017) DBSCAN parameters are closely related to the point spacing or in our case voxel size l_{min}. For our data and a l_{min} of 0.5 m, we found that a $r_{max} = l_{min}$ and v_{min} of seven results in a reasonable number of well-defined clusters. A larger search radius resulted in very few or single clusters that included most or all the changed voxels. When the minimum number of voxels was increased, too many change regions were misclassified as noise.

Another common challenge in change detection in underground MLS datasets is the geometric change in the mine drift floor due to mining operations such as mucking and leveling (Walton et al. 2018). Such change is not geotechnically relevant and can cause challenges for clustering relevant changes. We implemented a workflow to classify the mine drift floor to improve the clustering performance of DBSCAN. Similar to Ren et al. (2019) we use a Random Sample Consensus (RANSAC) algorithm (Fischler and Bolles 1981) to define the ground plane within the mine drift. We perform 1000 iterations of a plane fit to 500 voxels with normal vectors pointing in the positive z-direction. A threshold distance of l_{min} to the best fitting plane is used to classify all voxels as belonging to the mine floor. If floor voxels have been classified as changed, they can now be processed differently from changes in mine drift roof and wall voxels. In our case, we assign them to a distinct cluster before clustering other changes using DBSCAN.

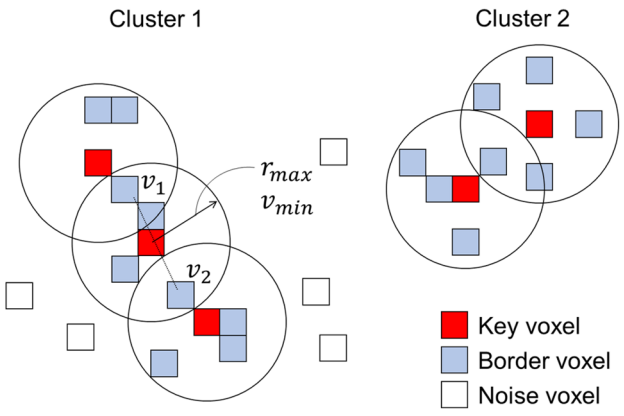

Fig. 7 The DBSCAN algorithm generated two clusters consisting of three types of voxels: key voxels (red), border voxels (blue), and noise voxels (white). Key voxels satisfy the cluster criteria of r_{max} and v_{min}, while border voxels do not meet the criteria but are within reach of a key voxel. Noise voxels do not belong to any cluster. The DBSCAN algorithm utilizes two rules: (1) voxels within r_{max} of a key voxel are considered part of its cluster, and (2) key voxels that share a common border voxel are considered part of the same cluster, as demonstrated by the example of v_1 and v_2 in Cluster 1. Adapted from Tonini and Abellan (2014), DiFrancesco et al. (2020) (Color figure online)

3 Results

3.1 Integration of Geological Faults into Change Detection

We processed the 9800 Level Access dataset, the 6700-01S datasets, and the regional fault model to investigate potential correlations of MLS-measured geometric changes and geological faults. Figure 8 shows the results for the two datasets.

The statistical analysis results to evaluate the potential correlation between MLS-measured changes and Euclidian distance to intersections with geological faults are shown in Fig. 9 and Table 1. For the 9800 Level Access, the mean Euclidian distance to a fault voxel intersection for unchanged voxels is 6.10 m and 5.90 m for changed voxels, with standard deviations of 3.80 and 4.30 m, respectively. The more outlier robust median shows a 0.9 m closer distance of changed voxels to faults compared to unchanged voxels. This represents a significant difference of unchanged and changed voxel distance to fault intersection of 15%. p values for the Mann–Whitney U test confirm this trend with a p value of 4.96e−12, suggesting a statistically significant difference at the 0.05 confidence level in the Euclidean distances of unchanged and changed voxels for 9800 Level Access dataset. We observe similar results for the 6700-01S dataset with a mean distance for unhanged voxels of 9.00 m and 8.30 m for changed voxels with standard deviations of 4.90 and 4.70 m, respectively. The median difference is similar to the 9800 Level Access data with 0.8 m between unchanged and changed voxels. This represents a statistically significant 9.00% difference between the two samples with a p value of 5.28e−15.

We also investigated the shortest path distance from an MLS voxel to a fault-MLS-voxel intersection and the Euclidian distance to the closest fault voxel. Figure 10a shows that for the full 6700-01S dataset, both distance metrics are comparable to the Euclidean distance to fault-MLS intersection and indicate slightly lower distances for changed voxels than unchanged voxels. The relative difference between the two metrics for unchanged and changed voxels is low. The

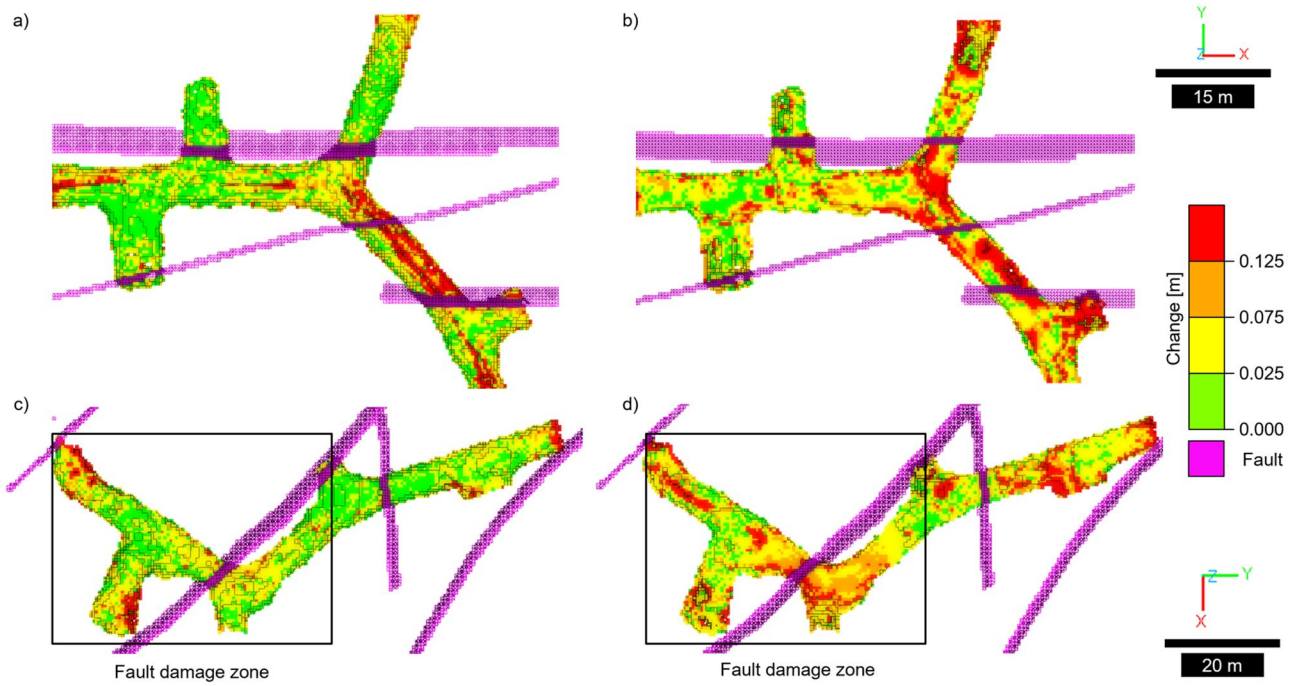

Fig. 8 Top and bottom view of 9800 Level Access (**a**, **b**) and 6700-01S (**c**, **d**) MLS data colored by change according to Kidd Mine Trigger Action Response Plan (TARP) and regional fault model. The fault damage zone shows significant changes near two faults

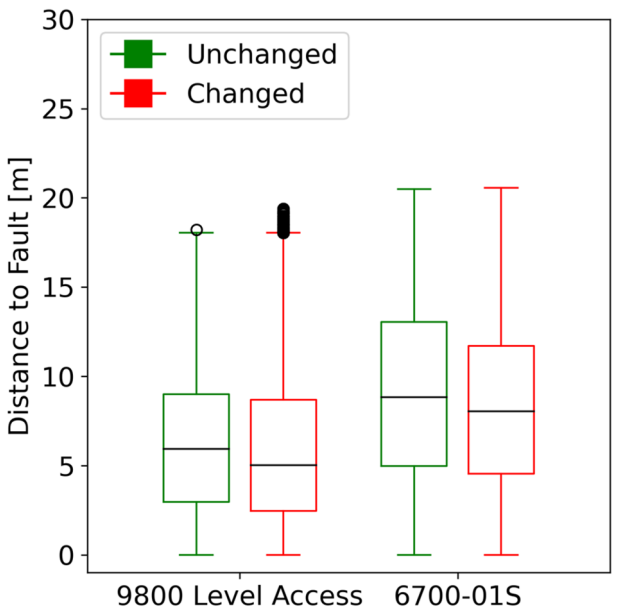

Fig. 9 Boxplot (left) showing the Euclidian distance to intersections between MLS and fault voxel of 9800 Level Access and 6700-01S MLS data by change classification

Euclidean distance to the closest fault voxel is lower, which is to be expected when faults run parallel to the mine drift, as in our dataset. The fault damage zone in Fig. 8 shows two faults intersecting the mine drift. Based on visual inspection, the fault damage zone shows a noticeably higher density of voxels with change magnitudes greater than 0.025 m near the intersection of the fault with the mine drift. This observation is supported by the analysis of boxplots for 6700-01S—Fault Damage Zone (Fig. 10b) and summary statistics in Table 2. They indicate an 18–30% closer mean distance of changed voxels to the nearest fault compared to unchanged voxels. We also investigated the use of alternative metrics considering multiple faults which did not show improvement in their ability to represent trends in change classification or magnitude.

We investigated a potential change magnitude and fault distance correlation based on the three distance metrics using binned mean and median plots shown in Fig. 11. In all metrics for the 6700-01S dataset, a trend towards larger magnitude changes occurring in closer proximity to fault intersection and fault voxels can be observed. The mean change magnitude decreases from almost 0.3 m at 0 m distance to fault intersections to below 0.05 m at the maximum distance recorded for each metric. As expected, the trend is more pronounced for changed voxels than for unchanged voxels where distance magnitudes remain relatively constant. The plots reveal a significant spike in the change magnitude for all metrics in the 12.5–22 m distance interval. This spike is most pronounced in the shortest connected path to fault intersection distance. Figure 12 uncovers that two areas with significant scan occlusion in one scan epoch fall within the distance interval. The

Table 1 Summary statistics for Euclidian distance to fault intersection for 9800 Level Access and 6700-01S

6700-01S-fault region—distance metrics (m)	9800 Level access		6700-01S	
	Unchanged	Changed	Unchanged	Changed
n	5939	8919	4478	7827
Mean	6.10	5.90	9.00	8.30
Median	5.90	5.00	8.80	8.00
Standard deviation	3.80	4.30	4.90	4.70
Mean absolute deviation	3.20	3.50	4.20	3.90
Unchanged to changed median % difference	−15.0		−9.00	
Mann–Whitney *U p* value unchanged/changed	4.96e−12		5.28e−15	

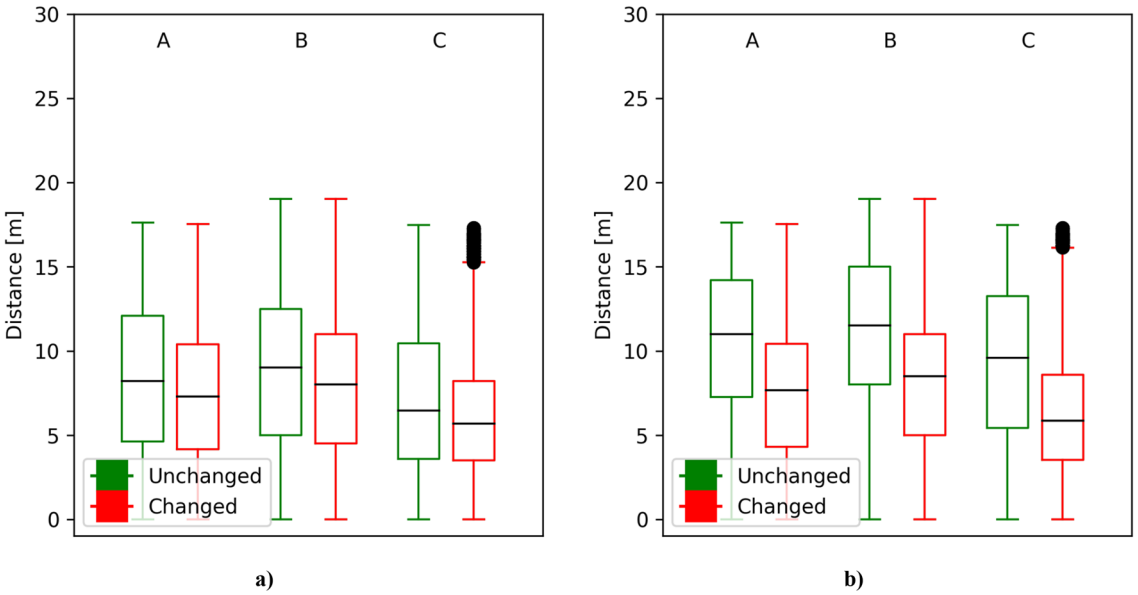

Fig. 10 Boxplots comparing A: Euclidian distance to fault-MLS intersecting voxels, B: Shortest connected path to intersecting voxels, and C: Euclidian distance to closest fault voxel for complete 6700-01S (**a**) and 6700-01S—Fault Damage Zone (**b**) data

Table 2 Summary statistics for the three MLS-to-fault-distance metrics for 6700-01S—Fault Damage Zone in meters

Voxel classification	A		B		C	
	Unchanged	Changed	Unchanged	Changed	Unchanged	Changed
Mean	11.00	8.80	12.00	9.80	9.30	6.5
Median	12.00	8.60	12.00	9.50	9.40	6.0
Standard deviation	4.70	4.90	5.30	5.80	4.40	3.80
Mean absolute deviation	3.90	4.10	4.30	4.60	3.70	3.00
Unchanged to changed mean % difference	−20.0%		−18.3%		−30.1%	

low density of points results in change distance computations that do not represent any meaningful changes in the mine drift geometry. If we remove the two occlusion areas in our analysis, the change magnitude spike within the 12.5–22 m interval is significantly reduced. We can observe a similar trend in the smaller fault damage zone section of the dataset.

For the full 6700-01S dataset, linear regression modeling for Min–Max normalized change magnitude and distance to fault did not reveal any meaningful trends. As shown in Fig. 13 and Table 3 for the 6700-01S—Fault Damage Zone dataset, the linear regression fit quality for changed voxels ($R^2 = 0.021$–0.043) is about twice as high as for unchanged voxels ($R^2 = 0.014$–0.019). When comparing difference in

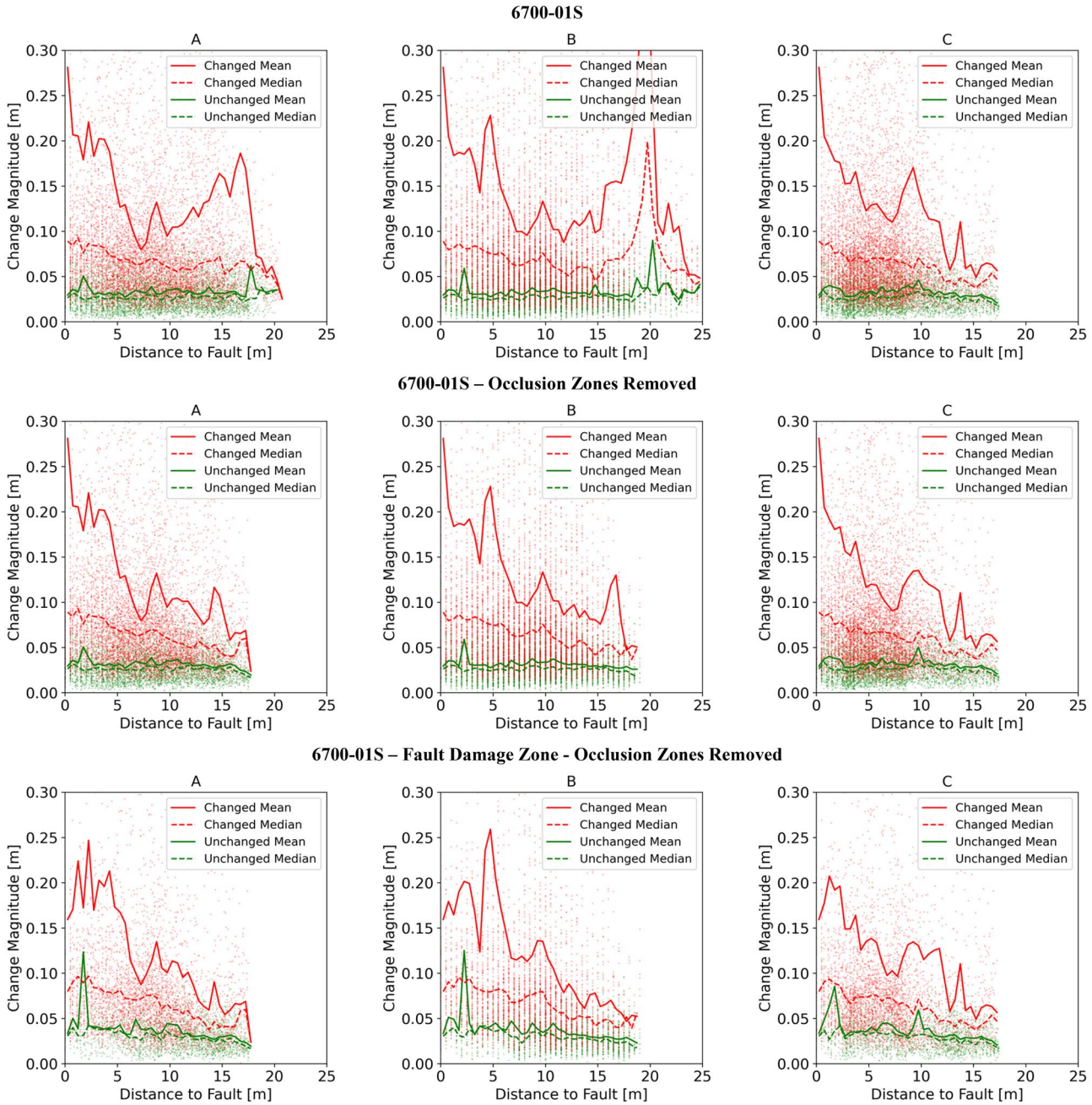

Fig. 11 Binned (0.5 m) mean and median fault distance compared to change magnitude for 6700-01S and 6700-01S—Fault Damage Zone datasets for unchanged and changed voxels. **A** Euclidian distance to fault-MLS intersecting voxels, **B** Shortest connected path to intersecting voxels, and **C** Euclidian distance to closest fault voxel

the regressions' slope magnitude, we observe that changed voxels exhibit a negative slope that is between 4–5 times steeper compared to the unchanged voxels. This difference indicates that voxels classified as changed show a more pronounced negative correlation between decreasing change magnitudes and increasing distance to fault intersection than unchanged voxels. We also investigated linear and logistic regression techniques to model both change magnitude and change classification in relation to fault distance, but the results remained largely inconclusive.

3.2 Integrated Analysis Using Microseismic, Geological, and MLS Data

We test the functionality of our geometric and combined attenuation models using the 9800 Level Access dataset with

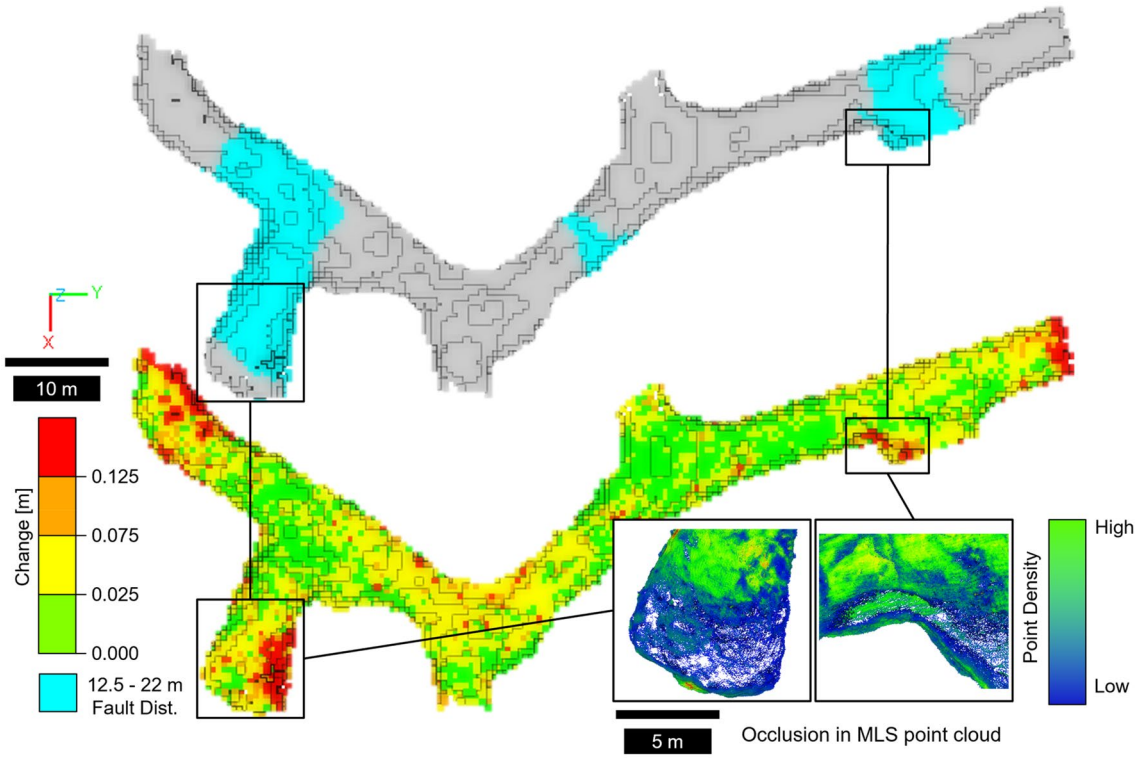

Fig. 12 Analysis of spiking change magnitude in the 12.5–22 m shortest connected path distance to fault-distance interval in the 6700-01S data. Both high change magnitude areas (> 0.125 m) correlate with high scan occlusion

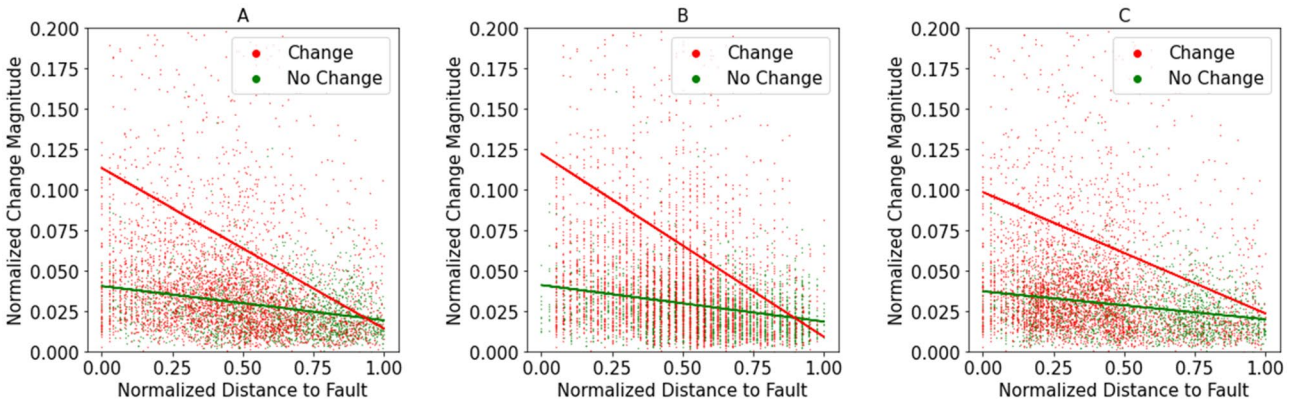

Fig. 13 Linear regression for three distance metrics. **A** Euclidian distance to fault-MLS intersecting voxels, **B** Shortest connected path to intersecting voxels, and **C** Euclidian distance to closest fault voxel for 6700-01S—Fault Damage Zone data with scan occlusion removed

Table 3 R^2 and slope values for linear regressions shown in Fig. 13

	A		B		C	
	Unchanged	Changed	Unchanged	Changed	Unchanged	Changed
R^2	0.018	0.040	0.019	0.043	0.014	0.021
Slope	−0.021	−0.099	−0.023	−0.113	−0.017	−0.075

A: Euclidian distance to fault-MLS intersecting voxels, B: Shortest connected path to intersecting voxels, and C: Euclidian distance to closest fault voxel

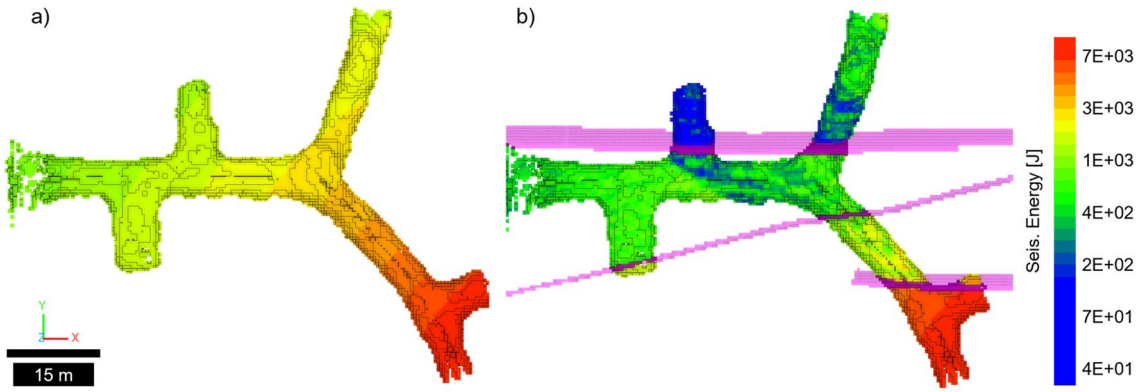

Fig. 14 Seismic energy exposure of 9800 Level Access based on seismic data from 07/31/2020 to 11/24/2020 for geometric attenuation model (**a**) and combined geometric and scattering attenuation model (**b**)

scans performed on 07/03/2020 and 11/24/2020 and all seismic events recorded in the same time interval. Figure 14 highlights the differences between the two models. In this period, the 9800 Level Access was primarily impacted by a significant 1.83 ML seismic event on 11/22/2020 at 1:41 AM that radiated 230 MJ. The event occurred close to the 9800 Level Access and about 50 m from the MLS scan region. The geometric model (a) shows the expected quadratically declining energy received by each MLS voxel within the MLS measurements interval between 07/31/2020 and 11/24/2020. The computed peak energy exposure is about 7 kJ. The combined geometric and scattering attenuation model (b) shows the same peak energy exposure and quickly declining seismic energy after each fault intersection.

We can observe significant outliers for all datasets and groups by analyzing the statistical distribution of normalized seismic energy for changed and unchanged voxel groups by fault model in Fig. 15 and the summary statistics in Table 4. Both models display significantly higher seismic energy in changed voxels than in unchanged voxels in Fig. 15a. The difference is more pronounced for the geometric model with more than 25% higher median seismic energy exposure in changed voxels than in unchanged. In the combined model, we only observe a 12% difference. The trend for mean and median in Fig. 15b shows an increase in change magnitude from 0.8 m to more than 0.15 m with increasing seismic energy exposure in the geometric attenuation model. This trend is not observable in the unchanged voxels, which remain relatively constant in change magnitude with increasing energy exposure. The linear regression model in Fig. 15b fitted to normalized seismic energy exposure in the geometric model to normalized change magnitude show a low R^2 value of 0.03 for the changed voxels. The slope indicates a positive correlation between seismic energy and change magnitude for changed voxels in our dataset, supporting the observations made from the previous plots.

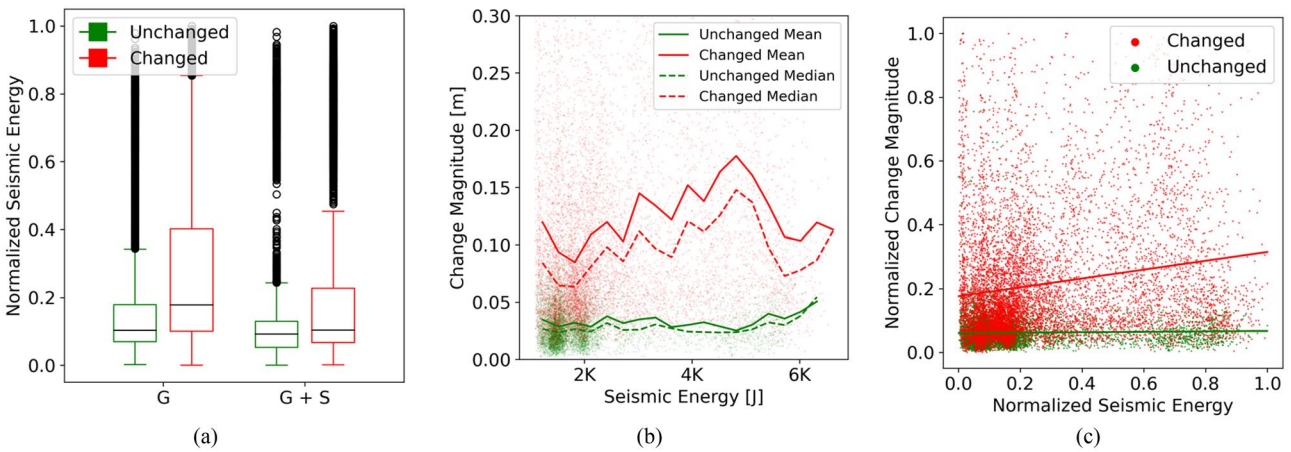

Fig. 15 Data-analysis for 9800 Level Access. Boxplots for normalized seismic energy for geometric and combined geometric and scattering attenuation (**a**). Mean and median seismic energy of 300 J wide bins compared to change magnitude < 0.5 m for geometric model (**b**). Linear regression for the geometric model fileted by 0.5 m change magnitude

Table 4 Summary statistics for seismic energy exposure modeling for 9800 Level Access

9800 Level Access seismic models	Geometric attenuation (J)		Geometric attenuation and fault scattering (J)	
	Unchanged MLS	Changed MLS	Unchanged MLS	Changed MLS
Mean	2064	2579	1065	1492
Median	1626	2042	635	714
Standard deviation	1114	1332	1401	1689
Mean absolute deviation	751	1088	876	1297
Unchanged to changed median change	26%		12%	
Mann–Whitney U p value unchanged/changed	1.52e−200		8.12e−75	

We also performed a multivariant analysis to investigate change magnitudes in relationship to their distance fault voxel and seismic energy exposure. Using the geometric attenuation model, we conducted this analysis for the 9800 Level Access and 6700-01S datasets. Figure 16 shows the results as binned means for Euclidean distance to faults and Euclidian distance to fault intersections. Building on our prior findings and site-specific knowledge, we hypothesize

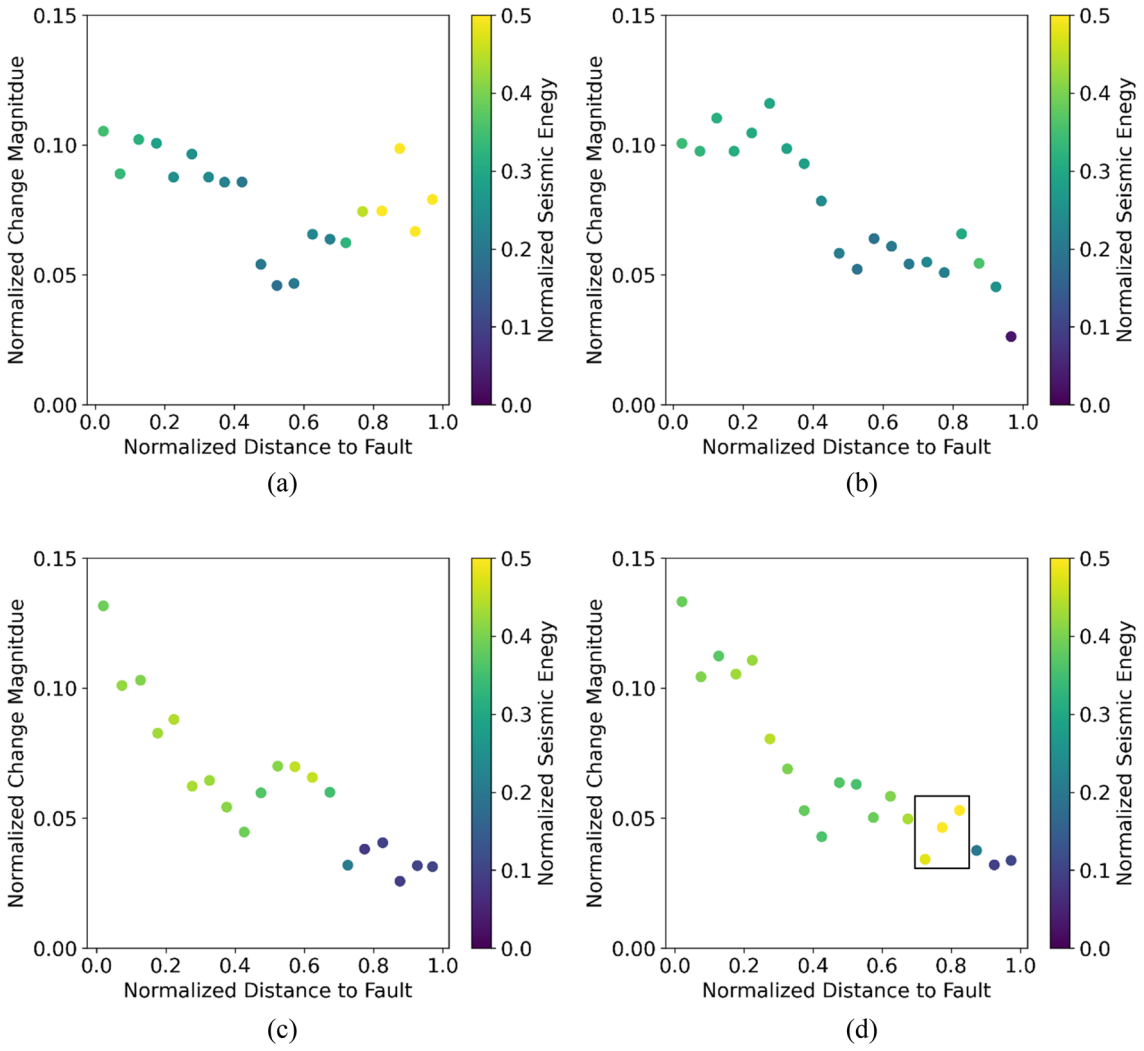

Fig. 16 Mean values of 0.05 wide bins over normalized distance to fault for 9800 Level Access (**a/b**) and 6700-01S (**c/d**) data. Euclidean distance to closest fault (**a/c**) and Euclidean distance to fault intersection voxel (**b/d**)

that higher change magnitudes may correlate with shorter distances to faults and increased seismic energy exposure. In Fig. 16a the 9800 Level dataset exhibits the same trend up to 0.6 on the normalized distance scale, after which both seismicity and change magnitudes rise again. Our hypothesis is further substantiated when assessing the distance to the closest fault intersection in Fig. 16b, where we observe a distinct trend of decreasing change magnitudes and seismicity as the distance to fault-drift intersections increases. This difference can be attributed to the fact that the geology of the 9800 Level is characterized by a fault running parallel to the drift section with no significant changes, while the most notable changes are observed near intersections with the fault.

For the 6700-01S dataset, we can observe a more uniform trend between the two distance metrics. While the data generally supports our hypothesis, Fig. 16d shows an increase in seismic energy at the 0.8 distance mark (box) which is not visible in the distance to the closest fault metric. The reason for this discrepancy can be observed in Fig. 17c, which corresponds to the highlighted points in the 0.8 distance interval in Fig. 16d. Due to the geometric configuration of the faults, the distance to fault intersection is significantly larger than the distance to any fault voxel and coincides with the region of the drift that also experienced a high seismic energy exposure.

3.3 Combined RANSAC and DBSCAN Approach for Semantic Clustering

To enhance the usability of MLS data, we improved the automated segmentation and implemented a new clustering approach (see Sect. 2.5). Figure 18a illustrates the function and output of the RANSAC implementation on the 6700-01S dataset. The set includes about 100 m of drift floor with a grade of 3.7%. Our method can correctly fit a plane to the ground plane and classify most voxels correctly as floor voxels. As shown in Fig. 18b, RANSAC does not classify 132 floor voxels (A), resulting in an F1 score of 0.985 (Table 5). The misclassification results from the uneven floor and the relatively large-scale plane fit, which could result in less reliable clusters if the goal is to remove floor voxels for further processing with DBSCAN and in analysis. One potential approach to address this issue is to fit multiple planes to smaller segments of the data to capture local irregularities in the mine floor better. The region in (B) does not include any MLS data, which results in missing floor voxels.

Figure 19 shows the combined RANSAC and DBSCAN output. After classifying floor voxels, we filter the dataset to include only those changes exceeding Kidd Mine's Trigger Action Response Plan (TARP) threshold of 0.025 m. We then perform DBSACN on the non-floor voxels, creating 36 clusters. The two largest change clusters are spatially well-correlated with the fault-drift intersections in (C). They also fall within a similar region as previously analyzed fault damage zone in Fig. 8.

4 Discussion

We performed a statistical analysis of the complete 9800 Level Access and the 6700-01S data investigating the distance of change and unchanged voxels to fault intersections. The results revealed a significant difference between the two groups with increasing change magnitudes being associated with decreasing distances to several fault-drift intersections. While the relative difference between the two voxel classes is significant and ranges from 9 to 15%, the absolute distance difference is small, ranging from 0.1 to 0.8 m, with a high standard deviation in the underlying distance metric (3.8–4.9 m).

The correlation between MLS-measured changes and proximity to fault-drift intersections is more pronounced in the 6700-01S—Fault Damage Zone subset than in the complete dataset. For this subset, we compared two alternative distance metrics: the shortest connected path from an MLS voxel to a fault intersection and the Euclidean distance to any fault voxel. The observed difference between the metrics of changed and unchanged voxels was 18–30% for the fault damage zone subset. This is two times higher compared to the complete 6700-01S. This finding indicates a scale-dependent, localized trend that becomes more discernible in

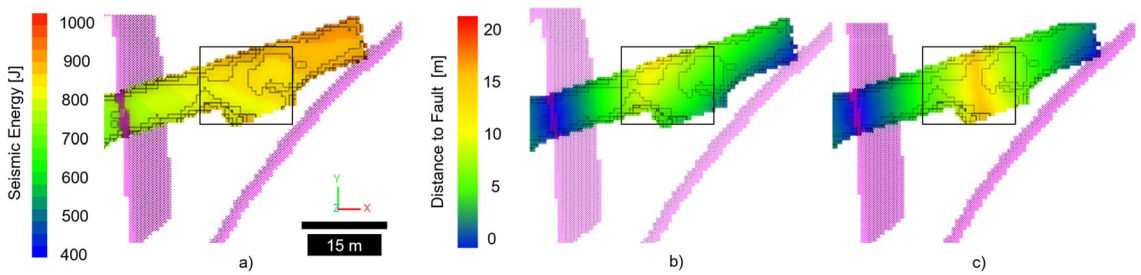

Fig. 17 Comparison of seismic energy exposure (**a**) to distance to closest fault (**b**) and closest fault intersection (**c**) for the 6700-01S data

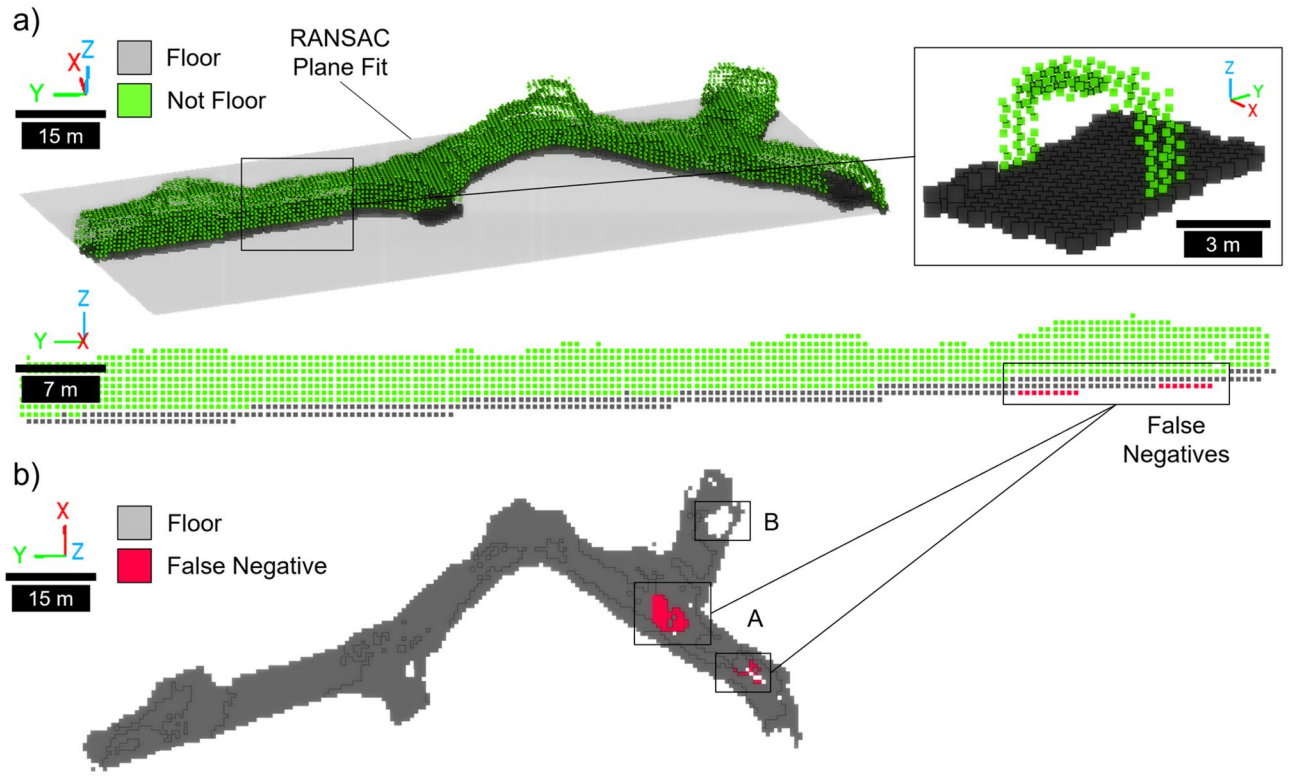

Fig. 18 Results of the RANSAC algorithm for 6700-01S data

Table 5 Confusion matrix for RANSAC classification for 6700-01S

	True Pos	True Neg	Sensitivity	Precision	F1
Pred. Pos	4324	0	0.870	1.000	0.9850
Pred. Neg	132	7849			

specific regions, such as zones directly influenced by faults. Geotechnical inspections at Kidd Mine by Black et al. (2021) support this idea and suggest that fault-related geotechnical changes can occur locally. Separating faults in our model into smaller units, e.g., based on their geological properties or orientation, has the potential to provide further insights. Our dataset reveals comparable results between the shortest connected path and Euclidean distance metrics. The former metric will likely be more significant in larger mine drifts, intricate drift networks, or fault-to-drift configurations. In such instances, investigating alternative metrics could be of added value.

The analysis of continuous change magnitudes supports the significant difference found in binary change classification of voxels and their distance to faults. Binned mean and median and linear regression analysis revealed decreasing change magnitudes with increasing distance to faults. An anomalous spike in change magnitudes at high fault distances could be attributed to occlusions in the MLS data, emphasizing the significance of obtaining dense and uniform lidar data (Fahle et al. 2022). As underscored by Fahle et al. (2020), adopting more automated, high-frequency MLS could be crucial in accomplishing this objective. As occlusion cannot always be avoided, reliable methods to filter occluded scan regions could further improve results.

Linear regression models indicated a trend that aligned with the findings from our other analyses. Their fit could be further improved by utilizing larger and high-density MLS datasets. In addition, shorter time intervals between MLS data collection would reduce the number of high-magnitude changes. Removing such potential outliers would also improve the fit of linear regression models. Our previous work demonstrated that high-density MLS data with a point spacing of 0.005 m collected in short intervals with higher-resolution MLS sensors, could deliver high-accuracy change detection (Fahle et al. 2022).The presence of non-linear behavior in the underlying trends, as evident by the moving averages, might constrain the quality of the linear fits. Lastly, it should also be considered that the geological fault locations derived from geological models carry inherent uncertainty. In the future, our framework could potentially be used to identify areas that might merit further geological mapping e.g., if MLS indicated changes and seismicity attenuation indicate a fault that has not yet been mapped.

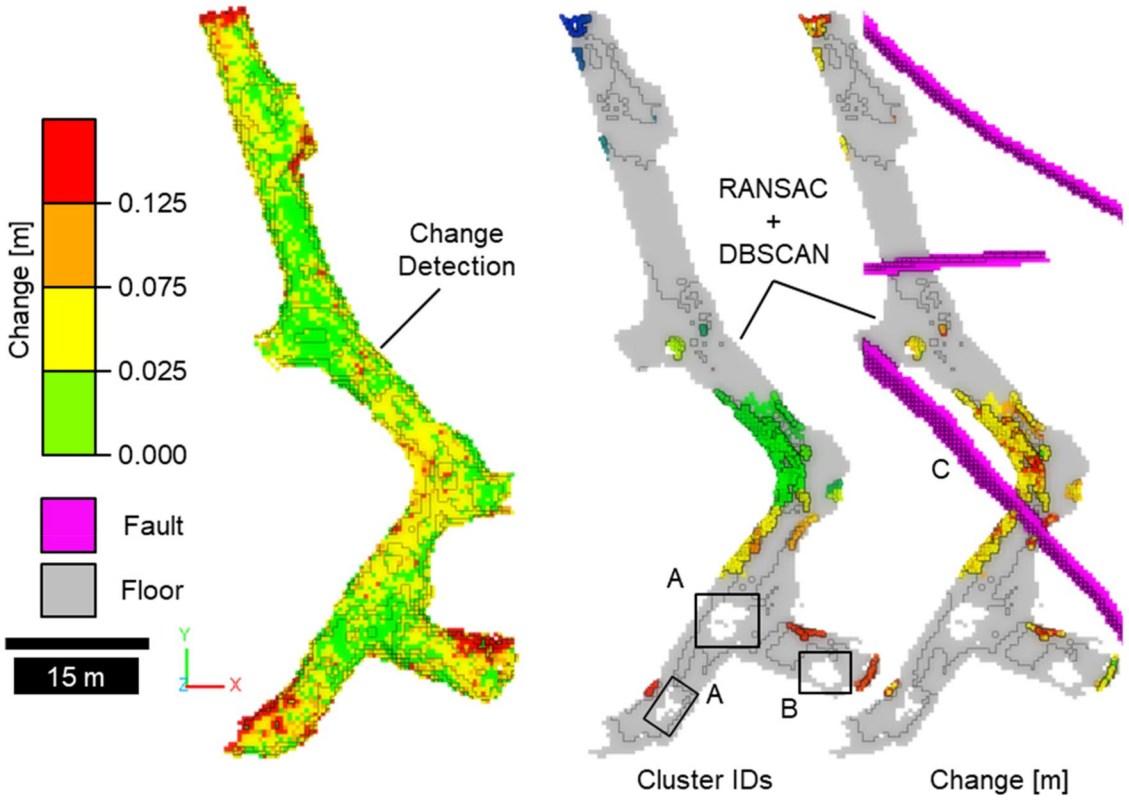

Fig. 19 Results of change detection, RANSAC floor classification, and DBSCAN clustering for 6700-01S. Some floor voxels are not correctly segmented (A). Area (B) with missing data in the MLS scan. The two largest change clusters show a good spatial correlation with the fault model and the previously identified fault damage zone (C)

Note that more frequent MLS scans were available but were not used in this analysis.

Our integration of seismic data with MLS data shows a statistically significantly higher energy exposure of changed MLS voxels relative to unchanged voxels. Analysis of change magnitudes also supports the hypothesis of increasing observable change magnitudes with increasing seismic energy exposure. The quality of the fit of a linear regression model is similar to the fault-distance model indicates a weak positive correlation between seismic energy and the change magnitude. Multivariate analysis for the 9800 Level Access and the 6700-01S datasets using binned means revealed a trend towards larger magnitude changes with decreasing distances to faults and increasing seismic energy exposure. These results align with studies that find positive correlations between seismic energy release and observed rockmass damage (Gale et al. 2001; Cai et al. 2001; Dehn et al. 2018). Our results also revealed that the strength of the correlation between seismic energy exposure and fault distance varies based on the chosen distance metric. This underscores that the selection of suitable metrics, interpretation of statistical results, and detection of trends are all inextricably linked to the local geological context.

Differences in seismic energy exposure in change and unchanged voxel varied based on the attenuation model. We found that this difference is more pronounced in the geometric attenuation model that does not consider scattering-based attenuation in fault zones. Geotechnical Engineers at Kidd Mine suggest that the fault movement measured by extensometers near the 9800 Level Access might have coincided with the seismic event on 11/22/2020 (Black et al. 2021). The described seismicity and correlated fault movements are likely associated with the MLS-measured changes observed in the rockmass. In this case, our implementation of faults as regions of high attenuation and lower seismic energy transmission might not correctly represent the fault zones and seismic energies' impact on the surrounding rockmass behavior. Integrating extensometer readings into our framework could provide additional data to calibrate our model and find a more suitable way of combining seismic energy release data and MLS-measured changes. Adding geological units to our model to better account for variations in Q-factor (Barton 2007) that could affect attenuation is another avenue for future research. Other metrics that have been utilized in other studies include seismicity, i.e., the rate of seismic events (Jones et al. 2014; Ma et al. 2016, 2020b)

and the Energy Index, i.e., the relationship of seismic energy to the seismic moment (Aswegen and Butler 1993; Dehn et al. 2018). These studies showed that both metrics could provide useful information on inferred stress levels for a given seismic volume and timeframe. In the future, we will investigate using such metrics in our framework, as they could also be used to prioritize regions for MLS surveys.

In the future, additional data types could be integrated into the analyses. For example, Kidd Mine is considering calibrating the deformation history of mine drifts and stopes to the ground support system's residual capacity (Counter 2019). Especially in fault zones that often require substantial ground support (Rahimi and Sharifzadeh 2017), the support's loading capacity can significantly impact the observable ground deformations (Bahrani and Hadjigeorgiou 2018; Rahimi et al. 2020). Examining the interplay among ground support, deformations, geology, and seismicity at a voxel level could offer more profound insights into complex and potentially non-linear correlations.

We combined RANSAC and DBSCAN methods within our framework to introduce more semantic understanding into an analysis workflow. Our approach demonstrates that we can automatically and accurately extract semantically relevant regions from MLS data, such as the mine floor and relevant change clusters. Our clustering-based approach improves visual inspection by automated filtering of potentially less relevant changes, including mine drift floor, low change magnitudes, and change clusters of low density. Similar to Evanek et al. (2021), Iannacchione et al. (2020), and Slaker et al. (2019) who primarily rely on visual inspections of lidar and geological fault data, we find that the generated clusters are spatially correlated with the geological fault model. Adding a combined RANSAC and DBSCAN method to our framework enables a more automated, less error-prone, and less biased analysis of changes. In the future, more advanced classification of clusters should be considered, as changes in the mine floor could, in some cases, be geotechnically-relevant floor heave.

Automating geotechnical data analysis will become even more important with increasing MLS data collection through autonomous mining vehicles (Fahle et al. 2020). We showed that our framework is an effective platform for such automated analysis, which could be further improved by using machine learning models for classification and prediction applications. Recent review articles indicate a scarcity of advanced machine learning applications in underground mine geotechnical engineering (Zhang et al. 2021, 2022; Kumar Singh et al. 2022), particularly in analyzing MLS-based change detection and geological data. One obstacle could be the lack of large datasets that combine MLS and geological data. As we demonstrated, our framework is well-suited for storing, pre-processing, and integrating such datasets. In the future, our framework could be used to test more complex machine learning models to explore relationships and predictive capabilities of MLS-measured changes and geotechnical input features. An interesting feature we have not explored in much detail is modeled and measured rock stress. In the future, results from stress measurements and numeric models could be incorporated into the voxel framework for integrated analysis with MLS-measured deformations, geological features, and seismicity.

5 Conclusion

This study presents an octree-based framework to perform geotechnical analysis that integrates geological, seismological, and MLS-based change detection data. We utilize an efficient statistical inference-based change detection approach in combination with additional octree data structures to store and process geological fault and seismic energy data. Our results indicate a statistically significantly lower distance of MLS-measured changed voxels to geological faults compared to unchanged voxels. In addition, our analysis reveals a statistically significant higher seismic energy exposure in changed MLS voxels than unchanged voxels for two tested attenuation models. To help automate the selection of regions of significant geotechnical change, we showcase the efficacy of a combined RANSAC and DBSCAN clustering workflow to remove potentially irrelevant changes in the mine floor and extract meaningful geotechnical change clusters. Our example shows a good spatial correlation of change clusters with geological data. We improved the understanding of geotechnical challenges at our case study site by contextualizing findings of our statistical-based analysis with site-specific knowledge. Our framework marks a substantial advancement in underground geotechnical monitoring and analysis. There are several opportunities for further improvement, including incorporation of higher spatiotemporal resolution MLS data, additional geological properties to enhance our seismic models, and exploration of advanced machine learning techniques to uncover non-linear relationships among geological, seismic, and MLS data. Overall, the integrated framework presented in this study advances MLS-based underground monitoring and geotechnical analysis by enabling statistical-driven analysis of multi-dimensional trends.

Acknowledgements This work was funded in part by the Alpha Foundation for mine safety under grant AFC820-54 and by the National Institute of Occupational Safety and Health (NIOSH) under Grant Number 200-2016-90154. We especially acknowledge Iain McKillip, James Comeau, and Megan Gidden at Kidd Mine for providing data and valuable discussion. We appreciate the comments of our anonymous reviewers to improve the quality of our manuscript.

Funding This study was funded by Alpha Foundation for the Improvement of Mine Safety and Health (No. AFC820-54) and National Institute for Occupational Safety and Health (No. 200-2016-90154).

Data availability Data used in this study has been provided by Kidd Mine and can be made available upon request.

Declarations

Conflict of interest The authors have no relevant financial or non-financial interests to disclose.

References

Aswegen GV, Butler AG (1993) Applications of quantitative seismology in South African gold mines. In: Young RP (ed) Proceedings of the 3rd international symposium on rockbursts and seismicity in mines, Kingston, pp 261–266

Bahrani N, Hadjigeorgiou J (2018) Influence of stope excavation on drift convergence and support behavior: insights from 3D continuum and discontinuum models. Rock Mech Rock Eng 51:2395–2413. https://doi.org/10.1007/s00603-018-1482-5

Barton NR (2007) Linking seismic velocity to rock quality Q and to seismic quality Q in the near-surface. In: 69th EAGE conference and exhibition incorporating SPE EUROPEC 2007. European Association of Geoscientists and Engineers, pp 332–337

Black D, Buckoll K, Maltais M et al (2021) Kidd Mine operations ground inspection report. Ateneo, Timmins

Brekke TL, Selmer-Olsen R (1966) A survey of the main factors influencing the stability of underground constructions in Norway. 1st ISRM Congress. OnePetro, Richardson

Bruneau G, Hudyma MR, Hadjigeorgiou J, Potvin Y (2003a) Influence of faulting on a mine shaft-a case study: part II-Numerical modelling. Int J Rock Mech Min Sci 40:113–125

Bruneau G, Tyler DB, Hadjigeorgiou J, Potvin Y (2003b) Influence of faulting on a mine shaft-a case study: part I-Background and instrumentation. Int J Rock Mech Min Sci 40:95–111

Cai M, Kaiser PK, Martin CD (2001) Quantification of rock mass damage in underground excavations from microseismic event monitoring. Int J Rock Mech Min Sci 38:1135–1145. https://doi.org/10.1016/S1365-1609(01)00068-5

CloudCompare (2021) CloudCompare. https://www.danielgm.net/cc/

Counter D (2014) Kidd Mine—dealing with the issues of deep and high stress mining—past, present and future. Proceedings of the seventh international conference on deep and high stress mining. Australian Centre for Geomechanics, Perth, pp 3–22

Counter D (2019) Laser-based scanning to manage geotechnical risk in deep mines. Proceedings of the ninth international symposium on ground support in mining and underground construction. Australian Centre for Geomechanics, Perth, pp 43–58

Dehn KK, Butler T, Weston B (2018) Using the energy index method to evaluate seismic hazards in an underground narrow-vein mine. In: 52nd US rock mechanics/geomechanics symposium, Seattle

DiFrancesco PM, Bonneau D, Hutchinson DJ (2020) The implications of M3C2 projection diameter on 3D semi-automated rockfall extraction from sequential terrestrial laser scanning point clouds. Remote Sens (basel). https://doi.org/10.3390/rs12111885

Dijkstra EW (1959) A note on two problems in connexion with graphs. Numer Math (heidelb) 1:269–271. https://doi.org/10.1007/BF01386390

Disley N (2014) Seismic risk and hazard management at Kidd Mine. Proceedings of the seventh international conference on deep and high stress mining. Australian Centre for Geomechanics, Perth, pp 107–121

Dunne K, Pakalnis RC (1996) Dilution aspects of a sublevel retreat stope at Detour Lake Mine. In: Rock mechanics tools and techniques, pp 305–313

Ester M, Kriegel H-P, Sander J, Xu X (1996) A density-based algorithm for discovering clusters in large spatial databases with noise. In: KDD, pp 226–231

Evanek N, Slaker B, Iannacchione A, Miller T (2021) LiDAR mapping of ground damage in a heading re-orientation case study. Int J Min Sci Technol 31:67–74. https://doi.org/10.1016/j.ijmst.2020.12.018

Fahle L, Holley E, Walton G (2020) Toward a mine-wide, real-time, and autonomous geotechnical change detection, monitoring, and prediction framework for underground mines. In: Klemetti T (ed) Proceedings of the 39th international conference on ground control in mining, ICGCM 2020. Society for Mining, Metallurgy, and Exploration (SME), Canonsburg

Fahle L, Carney P, Schiele S et al (2021) Evaluation of SLAM-based mobile lidar workflows and data quality for mine-wide underground geotechnical monitoring. 55th US rock mechanics/geomechanics symposium. OnePetro, Richardson

Fahle L, Holley EA, Walton G et al (2022) Analysis of SLAM-based lidar data quality metrics for geotechnical underground monitoring. Min Metall Explor. https://doi.org/10.1007/s42461-022-00664-3

Fahle L, Petruska AJ, Walton G et al (2023) Development and testing of octree-based intra-voxel statistical inference to enable real-time geotechnical monitoring of large-scale underground spaces with mobile laser scanning data. Remote Sens (basel) 15:1764. https://doi.org/10.3390/rs15071764

Fischler MA, Bolles RC (1981) Random sample consensus. Commun ACM 24:381–395. https://doi.org/10.1145/358669.358692

Gale WJ, Heasley KA, Iannacchione AT et al (2001) Rock damage characterisation from microseismic monitoring. Rock mechanics in the national interest. A.A. Balkema, Amsterdam

Goebel THW, Hauksson E, Aminzadeh F, Ampuero JP (2015) An objective method for the assessment of fluid injection-induced seismicity and application to tectonically active regions in central California. J Geophys Res Solid Earth 120:7013–7032. https://doi.org/10.1002/2015JB011895

Hamilton RM, Mooney WD (1990) Seismic-wave attenuation associated with crustal faults in the New Madrid seismic zone. Science 248:351–354

Hillers G, Campillo M, Ben-Zion Y, Roux P (2014) Seismic fault zone trapped noise. J Geophys Res Solid Earth 119:5786–5799. https://doi.org/10.1002/2014JB011217

Hu Z, Wu B, Xu N, Wang K (2022) Effects of discontinuities on stress redistribution and rock failure: a case of underground caverns. Tunn Undergr Space Technol 127:104583. https://doi.org/10.1016/j.tust.2022.104583

Iannacchione A, Miller T, Esterhuizen G et al (2020) Evaluation of stress-control layout at the Subtropolis Mine, Petersburg, Ohio. Int J Min Sci Technol 30:77–83. https://doi.org/10.1016/j.ijmst.2019.12.009

Jones E, Beck D, Villaescusa E (2014) The statistical presentation of seismicity for appreciating seismic hazard. Proceedings of the seventh international conference on deep and high stress mining. Australian Centre for Geomechanics, Perth, pp 659–666

Kaiser PK, Cai M (2012) Design of rock support system under rockburst condition. J Rock Mech Geotech Eng. https://doi.org/10.3724/sp.j.1235.2012.00215

King T, De Siena L, Benson P, Vinciguerra S (2022) Mapping faults in the laboratory with seismic scattering 1: the laboratory

perspective. Geophys J Int 232:1590–1599. https://doi.org/10.1093/gji/ggac409
Kumar SK (2022) Optimising mobile laser scanning for underground mines. University of New South Wales, Doctorate
Kumar Singh S, Pratap Banerjee B, Raval S (2022) A review of laser scanning for geological and geotechnical applications in underground mining. Int J Min Sci Technol. https://doi.org/10.1016/J.IJMST.2022.09.022
Lague D, Brodu N, Leroux J (2013) Accurate 3D comparison of complex topography with terrestrial laser scanner: application to the Rangitikei canyon (N-Z). ISPRS J Photogramm Remote Sens. https://doi.org/10.1016/j.isprsjprs.2013.04.009
Leake MR, Conrad WJ, Westman EC et al (2017) Microseismic monitoring and analysis of induced seismicity source mechanisms in a retreating room and pillar coal mine in the Eastern United States. Undergr Space 2:115–124. https://doi.org/10.1016/j.undsp.2017.05.002
Li S, Yu H, Liu Y, Wu F (2008) Results from in-situ monitoring of displacement, bolt load, and disturbed zone of a powerhouse cavern during excavation process. Int J Rock Mech Min Sci 45:1519–1525. https://doi.org/10.1016/j.ijrmms.2008.01.012
Lowrie W (2007) Fundamentals of geophysics, 2nd edn. Cambridge University Press, Cambridge
Luxbacher K, Westman E, Swanson P, Karfakis M (2008) Three-dimensional time-lapse velocity tomography of an underground longwall panel. Int J Rock Mech Min Sci 45:478–485. https://doi.org/10.1016/j.ijrmms.2007.07.015
Ma X, Westman EC, Fahrman BP, Thibodeau D (2016) Imaging of temporal stress redistribution due to triggered seismicity at a deep nickel mine. Geomech Energy Environ 5:55–64. https://doi.org/10.1016/j.gete.2016.01.001
Ma K, Zhang J, Zhou Z, Xu N (2020a) Comprehensive analysis of the surrounding rock mass stability in the underground caverns of Jinping I hydropower station in Southwest China. Tunn Undergr Space Technol 104:103525. https://doi.org/10.1016/j.tust.2020.103525
Ma K, Zhang J, Zhou Z, Xu N (2020b) Passive seismic imaging of stress evolution with mining-induced seismicity at hard-rock deep mines. Rock Mech Rock Eng 53:2789–2804. https://doi.org/10.1007/s00603-020-02076-5
Mann HB, Whitney DR (1947) On a test of whether one of two random variables is stochastically larger than the other. Ann Math Stat 18:50–60
Mark C, Molinda GM (2004) Preventing falls of ground in coal mines with exceptionally low-strength roof: two case studies. In: Peng SS, Mark C, Finfinger G et al (eds) 23rd international conference on ground control in mining
Meagher D (1982) Geometric modeling using octree encoding. Comput Graph Image Process 19:129–147. https://doi.org/10.1016/0146-664X(82)90104-6
Meglis IL, Chow T, Martin CD, Young RP (2005) Assessing in situ microcrack damage using ultrasonic velocity tomography. Int J Rock Mech Min Sci 42:25–34. https://doi.org/10.1016/j.ijrmms.2004.06.002
Mercer RA, Bawden WF (2005) A statistical approach for the integrated analysis of mine-induced seismicity and numerical stress estimates, a case study—part I: developing the relations. Int J Rock Mech Min Sci 42:47–72. https://doi.org/10.1016/j.ijrmms.2004.07.006
Mikula P (2020) The influence of geotechnical monitoring on mine design at Mt Charlotte. Geotechnical instrumentation and monitoring in open pit and underground mining. CRC Press, Boca Raton, pp 375–382
Möller T (1997) A fast triangle-triangle intersection test. J Graph Tools 2:25–30. https://doi.org/10.1080/10867651.1997.10487472
Nordlund E (2013) Deep hard rock mining and rock mechanics challenges. In: Potvin Y, Brady B (eds) Ground support 2013: proceedings of the seventh international symposium on ground support in mining and underground construction, Perth, pp 39–56
Oraee K, Oraee N, Goodarzi A, Khajehpour P (2016) Effect of discontinuities characteristics on coal mine stability and sustainability: a rock fall prediction approach. Int J Min Sci Technol 26:65–70
Palei SK, Das SK (2008) Sensitivity analysis of support safety factor for predicting the effects of contributing parameters on roof falls in underground coal mines. Int J Coal Geol. https://doi.org/10.1016/j.coal.2008.05.004
Puente I, Akinci B, González-Jorge H et al (2016) A semi-automated method for extracting vertical clearance and cross sections in tunnels using mobile LiDAR data. Tunn Undergr Space Technol 59:48–54. https://doi.org/10.1016/j.tust.2016.06.010
Rahimi B, Sharifzadeh M (2017) Evaluation of ground management in underground excavation design. Australian Centre for Geomechanics, Perth, pp 813–826
Rahimi B, Sharifzadeh M, Feng XT (2020) Ground behaviour analysis, support system design and construction strategies in deep hard rock mining—justified in Western Australian's mines. J Rock Mech Geotech Eng 12:1–20. https://doi.org/10.1016/j.jrmge.2019.01.006
Raval S, Banerjee BP, Singh SK, Canbulat I (2019) A preliminary investigation of mobile mapping technology for underground mining. IGARSS 2019–2019 IEEE international geoscience and remote sensing symposium. IEEE, pp 6071–6074
Ren Z, Wang L, Bi L (2019) Robust GICP-based 3D LiDAR SLAM for underground mining environment. Sensors 19:2915. https://doi.org/10.3390/s19132915
Sandbak LA, Rai AR (2013) Ground support strategies at the turquoise ridge joint venture, Nevada. Rock Mech Rock Eng 46:437–454. https://doi.org/10.1007/s00603-012-0342-y
Schiefer H, Schiefer F (2021) Statistics for engineers. Springer Fachmedien Wiesbaden, Wiesbaden
Shapiro SA, Kneib G (1993) Seismic attenuation by scattering: theory and numerical results. Geophys J Int 114:373–391. https://doi.org/10.1111/j.1365-246X.1993.tb03925.x
Slaker B, Murphy M, Winfield J (2019) Tracking convergence, spalling, and cutter roof formation at the pleasant gap limestone mine using LiDAR. In: 53rd US rock mechanics/geomechanics symposium
Slaker B, Murphy M, Rashed G et al (2020) Monitoring of multiple-level stress interaction at two underground limestone mines. Min Metall Explor. https://doi.org/10.1007/s42461-020-00345-z
Suorineni FT, Tannant DD, Kaiser PK (1999) Determination of fault-related sloughage in open stopes. Int J Rock Mech Min Sci 36:891–906. https://doi.org/10.1016/S0148-9062(99)00055-8
Szwedzicki T (2001) Geotechnical precursors to large-scale ground collapse in mines. Int J Rock Mech Min Sci 38:957–965. https://doi.org/10.1016/S1365-1609(01)00062-4
Terzaghi K (1942) Shield tunnels of the Chicago Subway. J Boston Soc Civ Eng 29:163–210
Tonini M, Abellan A (2014) Rockfall detectotion from terrestrial lidar point clouds: a clustering approach using R. J Spat Inf Sci 8:95–110. https://doi.org/10.5311/JOSIS.2014.8.123
Touma R, Aubry A, Ben-Zion Y, Campillo M (2022) Distribution of seismic scatterers in the San Jacinto Fault Zone, southeast of Anza, California, based on passive matrix imaging. Earth Planet Sci Lett 578:117304. https://doi.org/10.1016/j.epsl.2021.117304
Trifu CI, Suorineni FT (2009) Use of Microseismic Monitoring for Rockburst Management at Vale Inco Mines. In: Tang C (ed) Controlling seismic hazard and sustainable development of deep mines: 7th international symposium on rockburst and seismicity in mines. Rinton Press, New York, pp 1105–1114

Urbancic TI, Trifu CI (2000) Recent advances in seismic monitoring technology at Canadian mines. J Appl Geophys 45:225–237. https://doi.org/10.1016/S0926-9851(00)00030-6

van Veen M, Hutchinson DJ, Kromer R et al (2017) Effects of sampling interval on the frequency—magnitude relationship of rockfalls detected from terrestrial laser scanning using semi-automated methods. Landslides 14:1579–1592. https://doi.org/10.1007/s10346-017-0801-3

Vatcher J, McKinnon SD, Sjöberg J (2018) Rock mass characteristics and tomographic data. Rock Mech Rock Eng 51:1615–1619. https://doi.org/10.1007/s00603-018-1428-y

Walton G, Diederichs MS, Weinhardt K et al (2018) Change detection in drill and blast tunnels from point cloud data. Int J Rock Mech Min Sci 105:172–181. https://doi.org/10.1016/j.ijrmms.2018.03.004

Wang H, Xue S, Jiang Y et al (2018) Field investigation of a roof fall accident and large roadway deformation under geologically complex conditions in an underground coal mine. Rock Mech Rock Eng 51:1863–1883. https://doi.org/10.1007/s00603-018-1425-1

Westman EC, Molka RJ, Conrad WJ (2017) Ground control monitoring of retreat room-and-pillar mine in Central Appalachia. Int J Min Sci Technol 27:65–69. https://doi.org/10.1016/j.ijmst.2016.11.008

Wilhelms J, van Gelder A (1992) Octrees for faster isosurface generation. ACM Trans Graph 11:201–227. https://doi.org/10.1145/130881.130882

Williams K, Olsen MJ, Roe G, v., Glennie C, (2013) Synthesis of transportation applications of mobile LIDAR. Remote Sens 5:4652–4692

Xia K, Chen C, Wang T et al (2022) Investigation of mining-induced fault reactivation associated with sublevel caving in metal mines. Rock Mech Rock Eng 55:5953–5982. https://doi.org/10.1007/s00603-022-02959-9

Young RP, Maxwell SC (1992) Seismic characterization of a highly stressed rock mass using tomographic imaging and induced seismicity. J Geophys Res Solid Earth 97:12361–12373. https://doi.org/10.1029/92JB00678

Zhang W, Li H, Li Y et al (2021) Application of deep learning algorithms in geotechnical engineering: a short critical review. Artif Intell Rev 54:5633–5673. https://doi.org/10.1007/s10462-021-09967-1

Zhang W, Gu X, Tang L et al (2022) Application of machine learning, deep learning and optimization algorithms in geoengineering and geoscience: comprehensive review and future challenge. Gondwana Res 109:1–17. https://doi.org/10.1016/J.GR.2022.03.015

Zhao JS, Jiang Q, Lu JF et al (2022) Rock fracturing observation based on microseismic monitoring and borehole imaging: In situ investigation in a large underground cavern under high geostress. Tunn Undergr Space Technol 126:104549. https://doi.org/10.1016/j.tust.2022.104549

Zhen C, Qian S, Gui-min Z et al (2022) Response and mechanism of a tunnel subjected to combined fault rupture deformation and subsequent seismic excitation. Transp Geotech 34:100749. https://doi.org/10.1016/j.trgeo.2022.100749